JGR Space Physics

RESEARCH ARTICLE
10.1029/2024JA033545

Key Points:

- Comparison of Kaguya observations with a photoelectron energy spectral model provides horizontal variations of the lunar surface potential
- More positive potentials are identified in stronger crustal magnetic fields on the lunar dayside in the terrestrial magnetotail lobes
- The results imply the ubiquitous formation of upward electric fields above the crustal magnetic fields in various plasma regimes

Correspondence to:
M. Kato,
katomasa@kugi.kyoto-u.ac.jp

Citation:
Kato, M., Harada, Y., Saito, Y., Yokota, S., Nishino, M. N., Takahashi, F., et al. (2025). Inhomogeneous electrostatic potentials on the dayside lunar surface in the terrestrial magnetotail lobes: The role of lunar crustal magnetic fields. *Journal of Geophysical Research: Space Physics*, *130*, e2024JA033545. https://doi.org/10.1029/2024JA033545

Received 15 NOV 2024
Accepted 20 JAN 2025

Inhomogeneous Electrostatic Potentials on the Dayside Lunar Surface in the Terrestrial Magnetotail Lobes: The Role of Lunar Crustal Magnetic Fields

Masahisa Kato[1], Yuki Harada[1], Yoshifumi Saito[2], Shoichiro Yokota[3], Masaki N. Nishino[2], Futoshi Takahashi[4], Hisayoshi Shimizu[5], Shaosui Xu[6], Andrew R. Poppe[6], and Jasper S. Halekas[7]

[1]Department of Geophysics, Graduate School of Science, Kyoto University, Kyoto, Japan, [2]Institute of Space and Astronautical Science, Japan Aerospace Exploration Agency, Sagamihara, Japan, [3]Department of Earth and Space Science, Graduate School of Science, Osaka University, Osaka, Japan, [4]Department of Earth and Planetary Sciences, Faculty of Science, Kyushu University, Fukuoka, Japan, [5]Earthquake Research Institute, The University of Tokyo, Tokyo, Japan, [6]Space Science Laboratory, University of California, Berkeley, CA, USA, [7]Department of Physics and Astronomy, University of Iowa, Iowa City, IA, USA

Abstract Though the Moon does not possess a global magnetic field like the Earth, there are localized crustal magnetic fields on the lunar surface. Because of the plasma interaction with the crustal magnetic fields, electrostatic and electromagnetic environments near magnetized regions can differ from those near non-magnetized regions on the Moon. Previous studies observationally revealed the difference in the electrostatic potential on the lunar surface between magnetized and non-magnetized regions of the Moon in the solar wind, which was attributed to upward electric fields formed by electron-ion decoupling above the magnetic anomaly regions. However, these inhomogeneous distributions of surface potentials associated with lunar crustal magnetic fields remain uncharacterized in plasma regimes different from the solar wind. In this study, we use a large number of observations by Kaguya and a numerical model of photoelectrons emitted from the sunlit lunar surface to investigate the horizontal distributions of the lunar surface potential in the terrestrial magnetotail lobes. We estimate the relative surface potential variations from the measured energy shift of lunar surface photoelectrons. The results indicate that photoelectrons emitted from relatively strong crustal magnetic field regions tend to be more decelerated, suggesting more positive potentials on the magnetized surface. This implies that upward electric fields are formed by the interaction of terrestrial magnetotail plasma with the lunar crustal magnetic fields in a similar manner to the solar wind interaction with lunar crustal magnetic fields.

Plain Language Summary The magnetic field configuration on the Moon is very different from that of the Earth, which has a global magnetic field, and there are many localized strong magnetic fields of crustal origin, and they are called "magnetic anomalies." Because electrically charged particles interact with magnetic fields, previous studies reported that configurations of electric fields above the crustal magnetic field regions are different from those above non-magnetized regions. These differences can be caused by inhomogeneities of surface charging. Since surface charging alters environments of dust and electricity near the lunar surface, information on surface charging is very important for lunar surface exploration. In order to understand how the local surface charging is related to the crustal magnetic field regions and various environments of charged particles, we compared a large number of observations of electron energy spectra by spacecraft orbiting around the Moon and a numerical model that describes electron energy spectra. Our analysis suggests that the local surface charging and electric field configuration above the crustal magnetic field regions also exist when the charged particle environment is different from the previous studies. Our results also imply that the spatial distribution of magnetic anomaly can be important for lunar surface exploration.

1. Introduction

Since the Moon does not possess a dense atmosphere, the lunar surface directly interacts with its ambient plasma. The incoming or outgoing charged particles correspond to electric currents flowing into or out of the lunar surface. The imbalance between these currents causes the lunar surface charging, by which the lunar surface potential varies from the ambient plasma potential, and eventually, the net inward and outward currents balance at the equilibrium surface potential (Whipple, 1981). The lunar surface potential has been investigated by observations of charged particles. For example, Anderson et al. (1977) used the upward-traveling electrons to infer the presence of crustal magnetic fields. In the presence of both electric and magnetic fields above the lunar surface, loss cone distributions of upward-traveling electrons become energy dependent (Feldman et al., 1983). Utilizing these characteristics of electron distributions observed by the Lunar Prospector (LP), Halekas et al. (2002) revealed that the lunar nightside surface is negatively charged.

On the sunlit lunar surface, solar radiation drives the emission of photoelectrons and Auger electrons. Auger electrons are emitted from an outer shell of atoms when an electron at an the inner electron shell is emitted by injection of photons or energetic particles (Auger, 1925). The emitted Auger electrons have characteristic energies specific to the source atom and related electron shells. Lin and Gopalan (1991) proposed that the Auger electrons can be used as a remote sensing method targeting the chemical composition of the surface materials of airless bodies. Xu et al. (2021) reported observations of lunar Auger electrons from oxygen atoms by Acceleration, Reconnection, Turbulence, and Electrodynamics of the Moon's Interaction with the Sun (ARTEMIS) spacecraft (Angelopoulos, 2008) for the first time.

Meanwhile, Kato et al. (2023) developed a numerical model (hereafter referred to as the K23 model) of the energy spectrum of photoelectrons and Auger electrons emitted from the lunar surface by solar irradiation. The K23 model takes into account the solar irradiation flux, photoionization cross-sections of atoms, number densities of atoms, inelastic mean free path of surface material, probability distribution of the ejected electrons, escape efficiency of emitted electrons (which is the only free parameter and essentially acts as a scaling factor), and Auger yield of each element. Kato et al. (2023) report that the K23 model can successfully reproduce the ARTEMIS observations by adjusting the scaling factor.

Although the Moon does not possess a global intrinsic magnetic field, there are crustal magnetic field regions in places. Mitchell et al. (2008) remotely measured the magnetic field strength $|\boldsymbol{B}|$ on the lunar surface from LP observations of electron loss cones and showed that the maximum $|\boldsymbol{B}|$ exceeds 100 nT. The existence of the lunar crustal magnetic fields causes many complicated plasma interactions with the lunar surface and crustal fields. One consequence of the interactions is the difference in the lunar surface potential between magnetized and non-magnetized regions. Specifically, it has been suggested that more positive surface potentials are caused by upward electric fields formed above magnetized regions. Burke et al. (1975) used electron observations at the Apollo 14 landing site when the Moon was located in the terrestrial plasma sheet, and reported a surface potential of $+80$ V. This positive potential is much higher than a typical surface potential expected from a simple current balance and the observed additional potential was attributed to a charge separation electric field formed by the local crustal magnetic field of 75 nT. Saito et al. (2012) reported low-altitude ($\sim$25 km) ion and electron observations by Kaguya above a crustal magnetic field region in the solar wind and revealed that incoming electrons are accelerated and incoming ions are decelerated, thereby suggesting the formation of upward electric fields above the spacecraft resulting from decoupling of ions and electrons. Futaana et al. (2013) reported that the lunar surface potential becomes more positive in a crustal magnetic field region, using Energetic Neutral Atoms (ENAs) observations by Chandrayaan-1 when the Moon is in the solar wind. Yeo et al. (2022) investigated potential distributions around a magnetic dipole embedded below an insulating surface in a laboratory experiment, thereby simulating the solar wind interaction with lunar magnetic anomalies. These observations and experiments suggest that the upward electric field is formed as a result of plasma interaction with crustal magnetic fields. However, the surface potential distributions associated with lunar crustal magnetic fields have been mapped only for a specific magnetic anomaly region in the solar wind (Futaana et al., 2013) and Burke et al. (1975)'s plasma sheet results are based on the single landing site observations. Therefore, it remains unclear whether the formation of upward electric fields is ubiquitous for a wide variety of lunar crustal magnetic fields and in various plasma regimes.

Since many crustal magnetic field regions are located at mid and high latitudes, it is difficult to use ARTEMIS observations with nearly equatorial orbits to investigate global characteristics of surface potential distributions. Thus, in this study, we use observations by the polar orbit Kaguya spacecraft and compare Kaguya observations in the terrestrial magnetotail lobes with the K23 model to infer relative variations of lunar surface potentials from energy shifts of lunar surface photoelectrons.

This paper is organized as follows: Section 2 shows case studies of comparison between the Kaguya observations and the K23 model. Section 3 presents the statistical results of surface potential distributions using a large volume

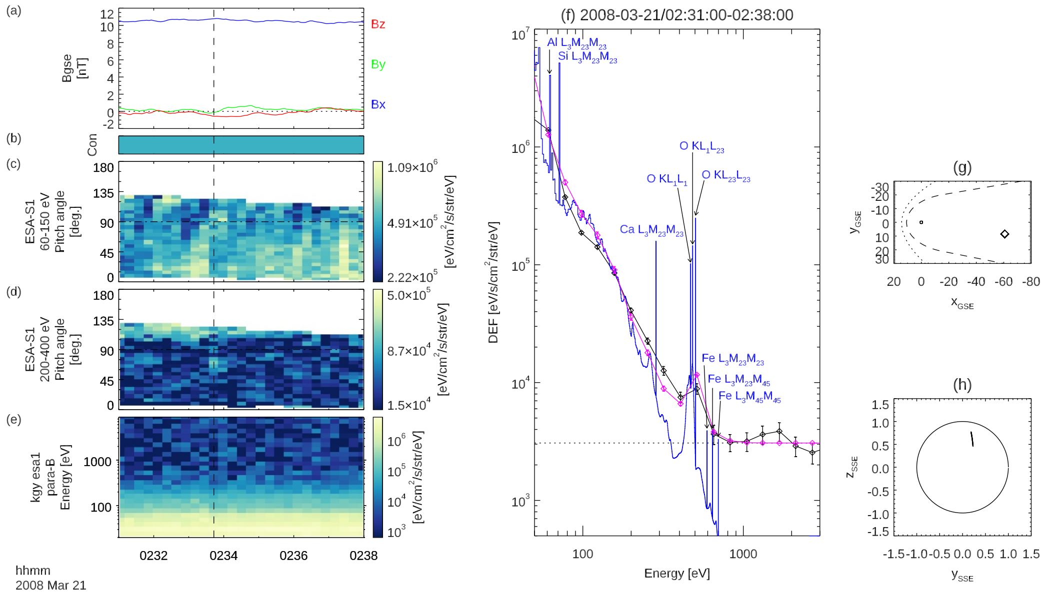

Figure 1. One example of the Auger electron observation by Kaguya in the terrestrial magnetotail on 20 March 2008. (a) Magnetic field in geocentric solar ecliptic (GSE) coordinates, (b) estimated magnetic field line connection to the Moon (light blue = connected), pitch angle distributions of electrons whose energies E are (c) $60 < E < 150$ eV and (d) $200 < E < 400$ eV, (e) energy spectra of electrons with $0° < \theta < 30°$, where θ indicates the pitch angle of the electrons, (f) the average energy spectra observed by Kaguya for the period (black), detailed energy spectra calculated by the K23 model (blue), and an estimated observation by accounting for the energy response of ESA1 onboard Kaguya (magenta) and the estimated background count level (the horizontal dashed line), and the positions of Kaguya in (g) GSE coordinates and (h) selenocentric solar ecliptic coordinates. We note that background counts are not subtracted in the ESA-S1 data shown in panels c, d, e, and f to highlight the weak signal of Auger electrons, while background counts are subtracted in the other ESA-S1 data presented in this paper.

of data obtained from January 2008 to June 2009. In Section 4, we discuss the interpretation of the spatial variations of the lunar surface potential, and Section 5 summarizes key conclusions.

2. Case Studies

We present several cases of comparison between electron observations by Kaguya above the sunlit lunar surface and the K23 model. Kaguya is a Japanese lunar orbiter launched in September 2007 (Kato et al., 2010). We use magnetic field data obtained by the Lunar MAGnetometer (LMAG) and electron data obtained by the Plasma energy Angle and Composition Experiment (PACE) (Saito et al., 2008) onboard Kaguya. In particular, we focus on the downward-looking Electron Spectrum Analyzer (ESA)-S1, which is suitable for observing upward-traveling photoelectrons emitted from the sunlit lunar surface.

We first investigate characteristic Auger electron signatures in Kaguya data to confirm that the detected upward electrons are dominated by lunar surface photoelectrons as previously reported from ARTEMIS observations (Xu et al., 2021). Figure 1 shows one example of the Auger electrons observed by Kaguya in the terrestrial lobe. Figures 1a and 1g show magnetic field data and Kaguya's position in geocentric solar ecliptic (GSE) coordinates, respectively. The dominant positive B_x component suggests that the Moon was located in the northern magnetotail lobe. During this time interval, Kaguya traveled in the northern hemisphere on the dayside of the Moon (Figure 1h). Figure 1b shows the magnetic field line connectivity of Kaguya to the Moon estimated from a straight field line extrapolation of the measured magnetic field direction. The light blue color indicates that Kaguya was magnetically connected to the dayside lunar surface throughout this period. This configuration is suitable for measuring lunar surface photoelectrons traveling upward along the field line. Figures 1c and 1d show pitch angle distributions of electrons at 60–150 eV and 200–400 eV, respectively. The lower-energy electrons show parallel (upward) electrons with broad pitch angles (Figure 1c), which are consistent with photoelectrons emitted from the dayside lunar surface (Harada et al., 2013; Xu et al., 2021). In the higher-energy electrons, we observe almost no prominent signals of magnetically reflected electrons except for the signal with pitch angles of 60°–75° at

02:33:43 UTC (the vertical dashed line in Figures 1a–1e). From these properties, we infer that the electrons moving along field lines with pitch angles <30° mainly consist of electrons emitted from the lunar surface with little contribution from magnetically reflected electrons in this case. Figure 1e shows the energy spectra of electrons at pitch angles of <30° observed by ESA-S1 and the average spectrum is shown by the black line in Figure 1f. Notably, we observe a peak at ∼500 eV in the electron energy spectrum albeit with a relatively low signal-to-noise ratio (Figure 1f). This peak is generally consistent with the predicted peak of oxygen Auger electrons from the K23 model (blue and magenta lines in Figure 1f). This suggests that Kaguya detected Auger electrons emitted from oxygen atoms of lunar surface materials despite the low solar activity in 2008. In addition to the Auger peak, we see that the general shape of the observed energy spectrum is roughly represented by the model spectrum within a factor of ∼2 discrepancy.

Having confirmed the K23 model can be used as a reference spectrum for the observed spectrum of lunar surface photoelectrons, we next compare the Kaguya observations with the K23 model and estimate the relative energy shift of lunar surface photoelectrons. The details are as follows. First, we determine the free parameter α in the K23 model. α represents the escape efficiency of photo-emitted electrons due to the surface roughness and essentially acts as a constant scaling factor of the entire spectrum. We estimate a global median of $\alpha = 0.420$ (the median absolute deviation is 0.104) based on α fitted for the individual orbits used in the statistical analysis described in Section 3. In this study, we fix $\alpha = 0.420$ to focus on the relative energy shift of the photoelectron spectrum and avoid the parameter degeneracy as described in Kato et al. (2023). We discuss potential limitations arising from this assumption in Section 4.

Next, we conducted chi-square fitting for an energy shift parameter ΔE between the K23 model-predicted spectrum and the energy spectrum observed by Kaguya at each time step. In this fitting, the chi-square is calculated by

$$\chi^2(\Delta E) = \sum_{i=i_{E_{\min}}}^{i_{E_{\max}}} \frac{(F_{o,i} - F_{m,i}(\Delta E))^2}{\sigma_{o,i}^2 + \sigma_{m,i}^2}, \tag{1}$$

where F_o is the differential energy flux of electrons observed by Kaguya at each time, and F_m is the differential energy flux of electrons calculated by the K23 model accounting for the energy resolution of ESA-S1. σ_o and σ_m are estimated errors of F_o and F_m, respectively. σ_o is estimated by counting statistics and σ_m is estimated by propagation of uncertainty in model inputs (Kato et al., 2023). In this paper, F_m is derived by convolving a smoothed model energy spectrum with the energy response of ESA-S1. Here the model spectrum is smoothed with a 10 eV width from the original 1 eV resolution spectrum before the instrument energy response convolution because we found that the combination of the peaky Auger features of the original model spectrum and ESA-S1's non-uniform energy response leads to a peculiar behavior of the fitting with ΔE. This smoothing effectively accounts for any temporal and/or spatial variations of the lunar surface potential within the measurement time and spatial resolutions. The time resolution of ESA-S1 is either 2 or 16 s depending on the operation modes, and the spatial resolution of lunar surface photoelectron measurements is mainly determined by the electron gyrodiameter (∼10 km for 100 eV electrons in a 7 nT magnetic field, here the gyrodiameter is twice the gyroradius) and by the spacecraft motion (∼1.5 km/s) within a single measurement. As will be shown in Figures 2c and 2d, we empirically determine the energy range ($E_{\max} = 150$ eV and $E_{\min} = 60$ eV) to eliminate contamination from magnetically scattered electrons.

Here we demonstrate our procedure to derive the relative energy shift by comparing Kaguya observations and the K23 model. Figure 2 shows one of the examples of Kaguya electron observations on 7 May 2009. The dominant negative B_x indicates that the Moon was located in the southern tail lobe (Figure 2c). During this time interval, Kaguya traveled from north to south over the nearside of the Moon (Figure 2f). The colored dots in Figure 2f indicate the magnetic field line footpoints on the lunar surface estimated from the straight field line extrapolation, which could introduce up to ∼30 km (corresponding to ∼1° latitude) mapping errors due to field line curvature (Mitchell et al., 2008). Figure 2b shows energy spectra of upward electrons with >150° pitch angles, while Figures 2c and 2d show pitch angle distributions of 60–150 eV and 200–400 eV electrons, respectively. After 11:36:41 UTC (dashed line in Figures 2a–2e) when Kaguya traveled over magnetized regions (Figure 2f), we observe relatively high fluxes of magnetically reflected electrons around 90°–120° in the 60–150 eV energy range (Figure 2c). Meanwhile, the pitch angle distributions of 200–400 eV electrons show similar signatures of

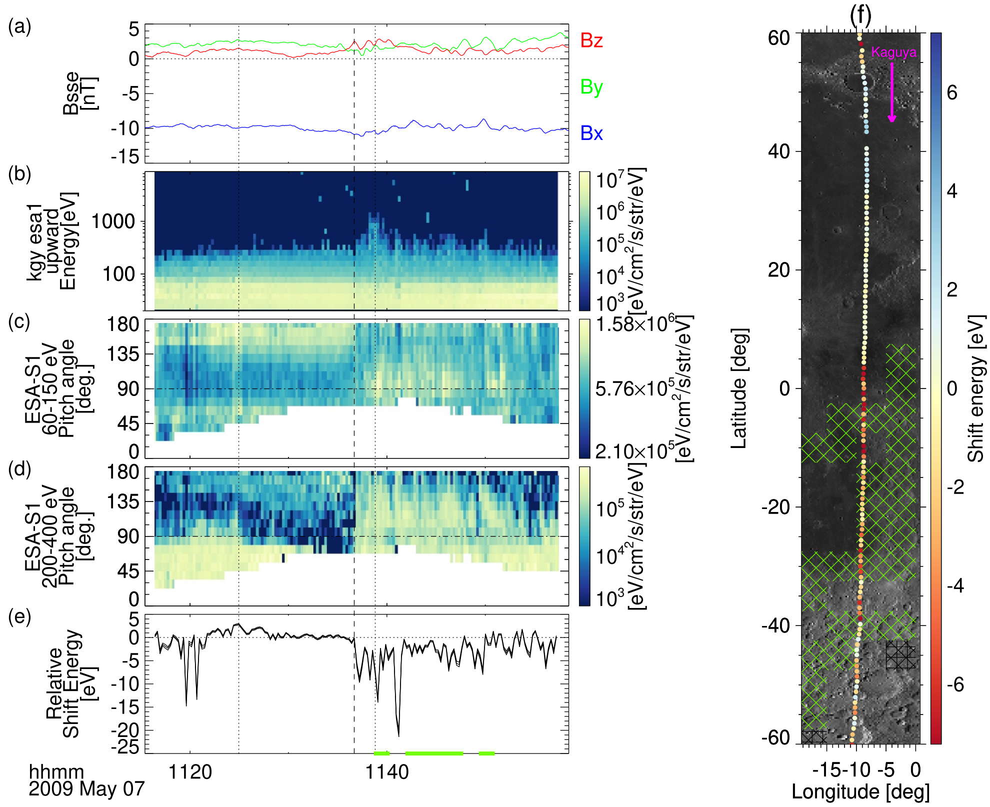

Figure 2. Overview of Kaguya observations on 7 May 2009 and the model calculation. (a) Magnetic field data in selenocentric solar ecliptic coordinates from LMAG, (b) energy-time spectrogram of upward (>150° pitch angles) electrons from ESA1, (c) and (d) pitch angle distributions of 60–150 eV and 200–400 eV electrons, respectively, (e) estimated relative energy shift of lunar surface photoelectrons by our method with the upper and lower lines indicating the uncertainty range of the fitting (see text in detail), and (f) the map of the field-line footprints of Kaguya superimposed on the lunar albedo map (Speyerer et al., 2011). The color scale in panel (f) indicates the relative energy shift shown in panel (e). The green hatched regions in panel (f) indicate relatively strong crustal magnetic field regions (magnetic field strength is greater than 2 nT inferred from electron reflectometry (Mitchell et al., 2008)) and the black hatched regions indicate data gaps of the electron reflectometry map. The vertical dashed lines indicate the times when characteristic spectra shown in Figure 3 were obtained. The bottom green bar in panel (e) indicates relatively strong crustal magnetic field regions corresponding to green hatches in panel (f). The magenta arrow in panel (f) indicates Kaguya's traveling direction.

relatively high fluxes extending to >135° pitch angles (Figure 2d). This can be explained by energy-dependent magnetic scattering (Halekas et al., 2010), by which higher-energy electrons with larger gyroradii are more susceptible to nonadiabatic scattering by short-wavelength crustal magnetic fields. These magnetically scattered electrons are sometimes seen in the upward (>150° pitch angles in this case) electron energy spectra (e.g., around 11:38:49 UTC indicated by the second vertical dotted line in Figure 2b), which complicate the interpretation of the photoelectron energy spectrum. Therefore, we utilize upward electron energy spectra in the 60–150 eV energy range as mentioned previously to focus on lunar surface photoelectrons. In Figure 2c, we observe higher fluxes of upward electrons with >150° pitch angles before 11:36:41 UTC than those after that. This suggests that Kaguya measured higher fluxes of lunar surface photoelectrons in the unmagnetized northern region than in the more magnetized southern region.

Figures 3a and 3c show examples of upward electron energy spectra obtained at 11:24:57 UTC in the unmagnetized region and 11:38:49 UTC in the magnetized region (indicated by the vertical dotted lines in Figure 2a–2e). The black lines show Kaguya observations and the magenta lines show the model-predicted spectra fitted to the observations by finding ΔE which gives the minimum χ^2 in the 60–150 eV energy range (indicated by the vertical dotted lines in Figures 3a and 3c). Figures 3b and 3d show χ^2 profiles as a function of ΔE. For the case shown in Figures 3a and 3b, the estimated relative energy shift ΔE is 2.9 eV, and for the case shown in Figures 3c and 3d,

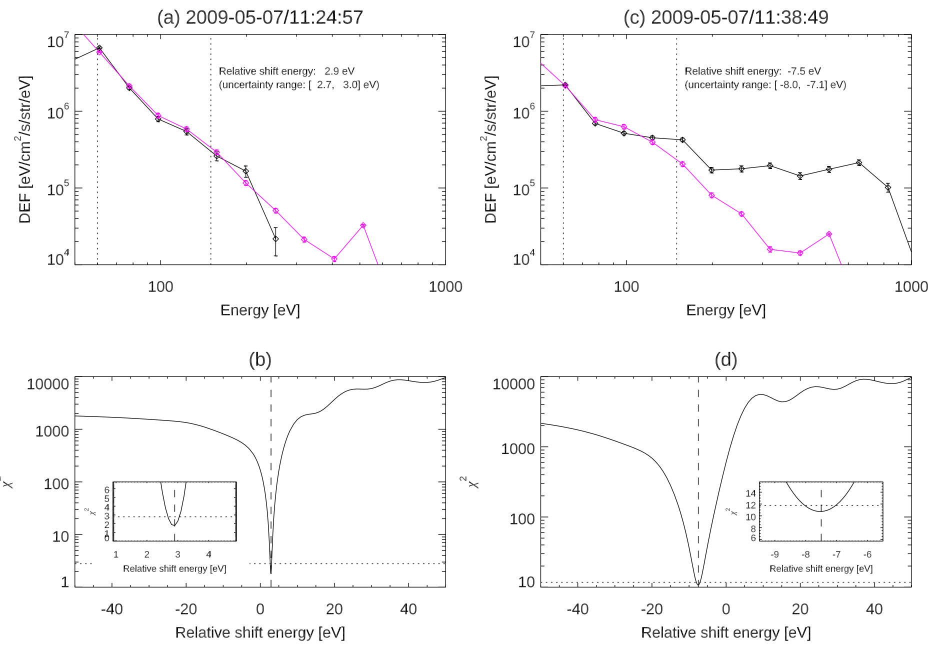

Figure 3. (a) and (c) Observed electron energy spectra of upward (>150° pitch angles) electrons at 11:24:57 UTC and 11:38:49 UTC (black lines), and virtual observations from the K23 model (magenta lines) with relative energy shifts $\Delta E = 2.9$ eV and $\Delta E = -7.5$ eV, respectively, (b) and (d) χ^2 profiles as a function of ΔE for the spectra at 11:24:57 UTC and 11:38:49 UTC, respectively. The subpanels in panels (b) and (d) are zoomed-in χ^2 profiles near $\min(\chi^2)$.

ΔE is -7.5 eV. We also estimate the uncertainty of the fitting parameter ΔE_e by searching the ΔE range which satisfies $\chi^2(\Delta E) < \min(\chi^2) + 1$, providing $2.7 \text{ eV} < \Delta E < 3.0 \text{ eV}$ for the case in Figures 3a and 3b and $-8.0 \text{ eV} < \Delta E < -7.1$ eV for the case in Figures 3c and 3d. We note that the upward electron flux at >150 eV is much higher than the model-predicted photoelectron flux in Figure 3c presumably because of the magnetically scattered electrons as discussed in the previous paragraph. The estimated ΔE in the magnetized region (Figure 3c) is more negative than that in the unmagnetized region (Figure 3a) as a consequence of the lower flux of upward electrons in the magnetized region inferring stronger electrostatic deceleration of the surface-emitted photoelectrons by more positive surface potentials. This difference can be also seen in the time series of the estimated energy shift ΔE in Figure 2e. ΔE tends to be more positive before 11:36:41 UTC and more negative after it. These differences generally correspond to the crustal magnetic field strength distribution (Figure 2f). We observe more negative ΔE (corresponding to more positive lunar surface potentials) with warm colors in the relatively strong crustal magnetic field region indicated by the green hatches in Figure 2f.

Figure 4 shows another example of Kaguya electron observations on 14 November 2008. In this period, Kaguya traveled from the southern hemisphere, where the crustal magnetic field strength is relatively strong, to the northern hemisphere, where there is almost no crustal magnetized region except for the well-known Reiner Gamma magnetic anomaly around ~10°N (Figure 4f). The dominant positive B_x component indicates that the Moon was located in the northern magnetotail lobe (Figure 4a). Overall, we observe lower fluxes of upward (parallel) electrons (Figures 4b–4d) and more negative ΔE (Figures 4e and 4f) above the relatively strong crustal magnetic field regions in a similar fashion to the orbit shown in Figure 2. Remarkably, the two depressions of upward electron flux and negative energy shift at 06:17:03–19 UTC and 06:18:07–23 UTC (dashed lines) in Figures 4b–4e correspond to the Reiner Gamma region with "swirl" albedo markings (Figure 4f). This suggests that the inferred deceleration of lunar surface photoelectrons is associated with crustal magnetic fields with relatively small spatial scales.

From these case studies, we identify more negative energy shifts (stronger deceleration) of lunar surface photoelectrons in stronger crustal magnetic field regions. To confirm whether this trend is general or specific to these events, we conduct a statistical study in the following section.

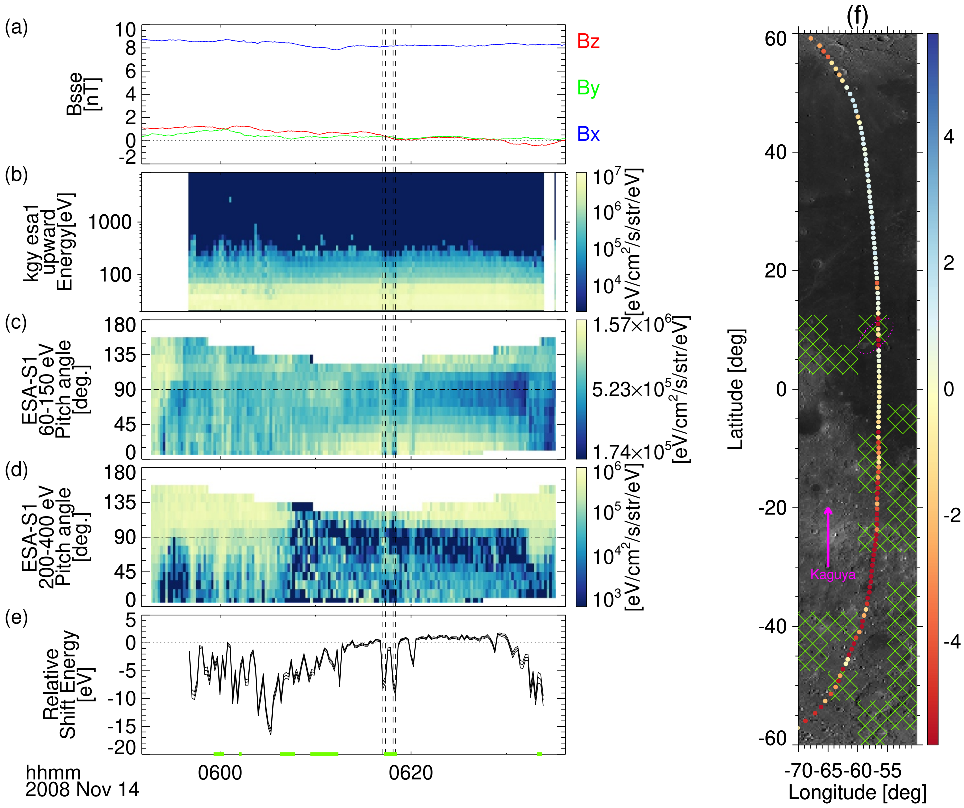

Figure 4. Overview of Kaguya observations on 14 November 2008 and the K23 model calculation in the same format as Figure 2. The magenta oval indicates the Reiner Gamma region with "swirl" albedo markings.

3. Statistical Results

We apply the same fitting method as the case studies shown in Section 2 to many dayside observations by Kaguya when the Moon was located in the lobe-like plasma regions. The dayside observations in lobe-like regions are selected according to the locations of the Moon and Kaguya, ion energy flux, and magnetic field strength as described in the following. First, we choose dayside observations in the terrestrial magnetotail that satisfy $0° < \phi < 70°$ and $150° < \psi < 210°$, where ϕ is the solar zenith angle of Kaguya and ψ is the angle between x axis in GSE coordinates and the direction of the Moon seen from the Earth. To further eliminate the magnetosheath and plasma sheet, we then exclude observations if the ion energy flux integrated between 300 eV and 1 keV exceeds 3.0×10^7 eV/cm^2/s/str or if $|B_{x,\mathrm{GSE}}| < 8$ nT, where $|B_{x,\mathrm{GSE}}|$ is the x component of the measured magnetic field in GSE coordinates. Applying these criteria, we identified 43,670 data points from 336 orbits. For each measurement, we estimate the source location of lunar surface photoelectrons by the straight magnetic field-line extrapolation as described in Section 2. Figure 5a shows a map of the estimated relative energy shift in the same format as Figure 2f. Overall, we see that the relative shift energy tends to be more negative (warm colors) in the relatively strong crustal magnetic field regions (green hatches) as suggested by the case studies presented in Section 2.

Additionally, we investigate the relationship between the crustal magnetic field strength and the energy shift of electrons. We obtain the magnetic field strength at each field-line footpoint from the 5° × 5° surface magnetic field strength map (Mitchell et al., 2008) derived by electron reflectometry based on LP observations. Since the map includes data gaps, some of the derived data points are excluded and we can use 42,197 points for the following analysis. Figure 5b shows histograms of the relative energy shift of lunar surface photoelectrons separated for different magnetic field strengths at the source locations. The energy shift distributions become skewed toward more negative energy shifts as the magnetic field strength increases, thereby demonstrating the

10.1029/2024JA033545

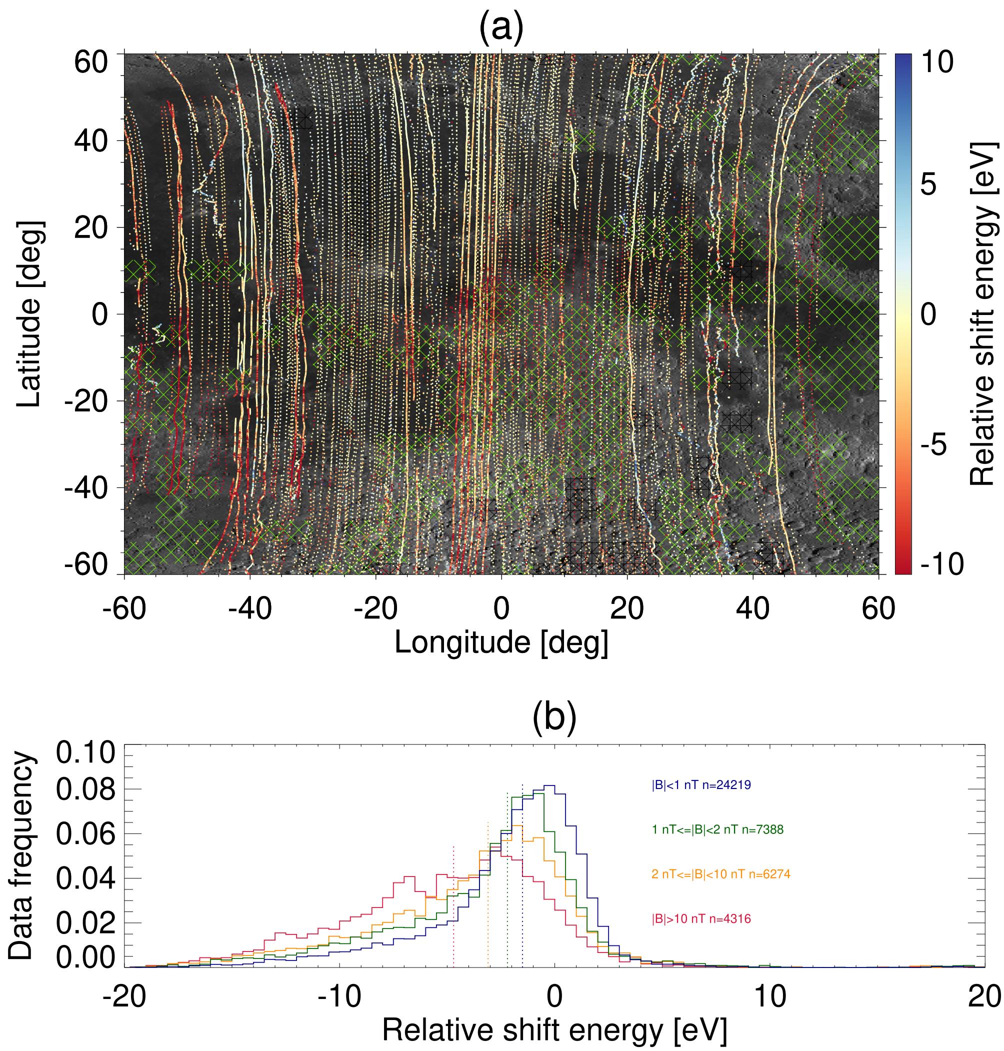

Figure 5. (a) The map of the estimated energy shift and (b) the histograms of the relative energy shift estimation for different crustal magnetic field strengths derived from Lunar Prospector observations (Mitchell et al., 2008). The vertical dashed lines indicate medians of the relative energy shift for different crustal magnetic field strengths.

aforementioned trend seen in the map. These statistical results shown in Figure 5 suggest that lunar surface photoelectrons emitted from magnetized regions are systematically more decelerated.

4. Discussion

As we have seen from the case studies and statistical results, lunar surface photoelectrons tend to be more decelerated above the relatively strong crustal magnetic field region. Assuming that the photoelectron energy shift is caused by an electrostatic potential variation, ΔU, we can infer that the lunar surface potential is more positive in relatively strong crustal magnetic field regions. It should be noted that the energy shift of the lunar surface photoelectrons is determined by the potential difference between the spacecraft and the lunar surface in principle. Since no spacecraft potential measurements are available for Kaguya, we cannot make corrections for the spacecraft potential variations that possibly affect ΔU. However, the relative energy shift map (Figure 5a) shows coherent selenographical patterns associated with lunar crustal magnetic fields. It is hard to explain these systematic trends merely by the variations of the spacecraft potential, which is mainly determined by the current balance among the spacecraft photoelectrons, ambient electrons, and ions. Therefore, we can reasonably infer that the systematic variations of the relative energy shift of lunar surface photoelectrons seen in Figure 5 are more likely to be caused by the spatial variations of the lunar surface potential rather than temporal variations of the spacecraft potential. We find several exceptions of relatively large negative energy shifts observed in regions without the green hatches in Figure 5a. For example, the negative energy shift is seen between $\sim -30°$ and $-35°$ longitude and $\sim -10°$ and $-50°$ latitude. This region is populated by weak, but non-zero, crustal magnetic fields as seen in Plate 1 of Halekas et al. (2001) and Figure 4 of Mitchell et al. (2008). We speculate that such weak magnetic fields could partly account for the observed negative energy shifts. According to Figure 5, the lunar surface potential variations between non-magnetized regions and relatively strong crustal magnetic field regions are on the order of $\Delta U \lesssim 10$ V.

We compare these results with previous studies. Qualitatively, this trend is consistent with previous studies that suggest the existence of upward electric fields above lunar crustal magnetic fields (Burke et al., 1975; Futaana et al., 2013; Saito et al., 2012). It is proposed that the upward electric field is formed by the Hall effect and charge separation based on theoretical calculations (e.g., Saito et al., 2012), hybrid simulations (e.g., Fatemi et al., 2015; Jarvinen et al., 2014) and kinetic simulations (e.g., Deca et al., 2015; Usui et al., 2017). Meanwhile, ΔU inferred in this study is much smaller compared to the previous studies. Burke et al. (1975) suggested that $\Delta U \approx 50$–70 V at the Apollo landing site when the Moon was located in the terrestrial plasma sheet. Futaana et al. (2013) estimated that $\Delta U \approx 150$ V by observations of ENAs when the Moon was located in the solar wind.

Here we discuss possible reasons for the discrepancy of the magnitude of ΔU between this analysis and the previous studies. First, since our study estimates the surface potential by remote measurements using lunar surface photoelectrons gyrating around the magnetic field line, the estimated surface potential for each measurement in orbit is averaged over the area characterized by the electron gyrodiameter (~ 10 km). Thus, any large potential at a single site (e.g., at the Apollo landing site) could be smoothed out over a wide area by the Kaguya remote measurements.

Second, the crustal magnetic fields in the previous studies ($|\boldsymbol{B}| \sim 75$ nT) at the Apollo landing site investigated by Burke et al. (1975) and $|\boldsymbol{B}| \lesssim 100$ nT for the Gerasimovic magnetic anomaly studied by Futaana et al. (2013) are much stronger than most of the crustal magnetic fields surveyed in this study ($|\boldsymbol{B}| \lesssim 10$ nT, Figure 5b). According to a numerical simulation (Poppe et al., 2012), the magnitude of ΔU increases with increasing $|\boldsymbol{B}|$, which is qualitatively consistent with the ΔU discrepancy seen here.

Third, while Futaana et al. (2013) and Burke et al. (1975) focus on the solar wind and terrestrial plasma sheet, respectively, our analysis utilizes observations in the terrestrial magnetotail lobes. The differences in plasma parameters could lead to the generation of upward electric fields with different magnitudes. Poppe et al. (2012) simulated the interaction between the solar wind and magnetic anomalies on the lunar surface, thereby deriving the ratio of the maximum electrostatic potential energy to the incident solar wind bulk energy as a function of crustal magnetic field strength. If we assume that this modeled relationship is also valid in plasma regimes other than the solar wind, the magnitude of ΔU in the tail lobes could become smaller even if the ratio of the potential energy to the incident bulk energy remains the same because the bulk energy of lobe ions is generally low compared to the solar wind and plasma sheet ions.

It should be noted that we only focus on the effects of the surface magnetic field strength on the inferred potential distributions since we use the electron reflectometry map (Mitchell et al., 2008). As discussed in Hemingway and Garrick-Bethell (2012) and Vorburger et al. (2012), the direction and spatial extent of local magnetic fields are additional factors that can affect the charged particle motion and resulting potential distributions. In future work, the dependences of surface potential distributions on the different aspects of the lunar crustal magnetic fields should be investigated in more detail.

We also investigate another possible factor that could contribute to the systematic selenographic distributions of the inferred relative energy shift of lunar surface photoelectrons: the difference in surface material properties between the highland and mare regions. To distinguish the dependences on the compositional difference and the lunar crustal magnetic fields, we divide the data into four groups according to the surface magnetic field strength (Mitchell et al., 2008) and Fe weight density (the highland (mare) corresponds to the Fe poor (rich) region) in 5-degree elemental abundance data products (Prettyman et al., 2002) derived from LP gamma ray spectrometer (Feldman et al., 1999) as shown in Table 1. In a given Fe poor/rich group (column), the median relative energy shift is consistently more negative in the strong $|\boldsymbol{B}|$ group. In a given $|\boldsymbol{B}|$ group (row), the median relative energy shift is more negative in the Fe poor group, but the difference is less prominent than the $|\boldsymbol{B}|$ dependence. Based on these results, we conclude that the lunar crustal magnetic field strength is a stronger controlling factor of the

Table 1
Median Energy Shift in eV for Different Fe wt% and $|\boldsymbol{B}|$ Groups

	Fe poor ($\rho < 10$wt%)	Fe rich ($\rho \geq 10$wt%)
Strong $|\boldsymbol{B}|$ ($|\boldsymbol{B}| \geq 1$ nT)	$-3.1^{-0.9}_{-7.0}$ ($n = 13094$)	$-2.7^{-0.9}_{-5.9}$ ($n = 4884$)
Weak $|\boldsymbol{B}|$ ($|\boldsymbol{B}| < 1$ nT)	$-1.7^{+0.1}_{-4.8}$ ($n = 9285$)	$-1.4^{+0.1}_{-3.1}$ ($n = 14934$)

Note. The superscript and subscript indicate the upper and lower quartiles for each group, respectively.

inferred energy shift of lunar surface photoelectrons compared to the compositional difference of the surface material.

Finally, we discuss another limitation of applying our methodology to Kaguya data. Since no Auger features are well resolved by ESA-S1 in the energy range of 60–150 eV, we essentially use the continuum spectrum of lunar surface photoelectrons to infer the relative energy shift. This leads to the aforementioned parameter degeneracy between α (overall flux scaling) and ΔE (energy shift). If our assumption of constant α is invalid and α varies systematically with lunar crustal magnetic fields for some reason, the parameter degeneracy introduces ambiguity in our interpretation of attributing the measured lunar photoelectron variations solely to lunar surface potential variations. This is a fundamental limitation of using electron measurements with insufficient energy resolution, although we currently do not have a physical expectation for α variations with lunar crustal magnetic fields. This ambiguity should be solved with future high-energy resolution measurements of Auger electrons, which provide a direct measure of acceleration and deceleration between the surface and the instrument.

5. Conclusions

We presented Kaguya ESA-S1 observations of photoelectrons emitted from the sunlit lunar surface in the terrestrial magnetotail lobes. We compared ESA-S1 observations of lunar surface photoelectrons in the tail lobes with the energy spectral model of lunar surface photoelectrons, namely the K23 model. In the Kaguya data, we identified a flux peak at energies around 500 eV indicative of Auger electrons from oxygen atoms as reported from ARTEMIS observations by Xu et al. (2021). Based on case studies and statistical analysis, we identified that the lunar surface photoelectrons emitted from relatively strong crustal magnetic field regions are more decelerated than those emitted from non-magnetized regions. We interpret this as electrostatic deceleration by upward electric fields formed above the magnetized regions of the Moon in the magnetotail lobes. The presence of upward electric fields above magnetized regions was pointed out by the previous studies from orbiter observations in the solar wind and from single landing site observations in the terrestrial magnetotail plasma sheet, and our results in the tail lobes imply that the formation of upward electric fields above the crustal magnetic fields is common in various plasma environments. Taken together, these results indicate the spatial inhomogeneity of the lunar surface potential associated with lunar crustal magnetic fields and its temporal variability because of the variable lunar plasma environment.

Data Availability Statement

Kaguya data used in Figures 1c–1f are archived in Kato et al. (2024) The other Kaguya data used in this paper are available (Kaguya-project, 2017). Data processing was done using SPEDAS (Angelopoulos et al., 2019). 5-degree Fe abundance data products (Prettyman et al., 2002) are available at https://pds-geosciences.wustl.edu/missions/lunarp/reduced/iron5d.txt.

Acknowledgments
MK was supported by JST SPRING, Grant JPMJSP2110. YH acknowledges support through JSPS KAKENHI Grant (JP22K14085, JP22H01285, JP22KK0045). MK is supported by Takenaka Scholarship Foundation. MK wishes to thank Kumano dormitory community at Kyoto University for their generous financial and living assistance.

References

Anderson, K., Lin, R., McGuire, R., McCoy, J., Russell, C., & Coleman, P. (1977). Linear magnetization feature associated with Rima Sirsalis. *Earth and Planetary Science Letters*, *34*(1), 141–151. https://doi.org/10.1016/0012-821X(77)90115-7

Angelopoulos, V. (2008). The THEMIS mission. *Space Science Reviews*, *141*(1–4), 5–34. https://doi.org/10.1007/s11214-008-9336-1

Angelopoulos, V., Cruce, P., Drozdov, A., Grimes, E. W., Hatzigeorgiu, N., King, D. A., et al. (2019). The space physics environment data analysis system (SPEDAS). *Space Science Reviews*, *215*(1), 9. https://doi.org/10.1007/s11214-018-0576-4

Auger, P. (1925). Sur l'effet photoélectrique composé. *Journal de Physique et le Radium*, *6*(6), 205–208. https://doi.org/10.1051/jphysrad:0192500606020500

Burke, W. J., Reiff, P., & Reasoner, D. (1975). The effect of local magnetic fields on the lunar photoelectron layer while the moon is in the plasma sheet. In *Lunar and Planetary Science Conference Proceedings* (Vol. 6, pp. 2985–2997).

Deca, J., Divin, A., Lembège, B., Horányi, M., Markidis, S., & Lapenta, G. (2015). General mechanism and dynamics of the solar wind interaction with lunar magnetic anomalies from 3-D particle-in-cell simulations. *Journal of Geophysical Research: Space Physics*, *120*(8), 6443–6463. https://doi.org/10.1002/2015JA021070

Fatemi, S., Lue, C., Holmström, M., Poppe, A. R., Wieser, M., Barabash, S., & Delory, G. T. (2015). Solar wind plasma interaction with Gerasimovich lunar magnetic anomaly. *Journal of Geophysical Research: Space Physics*, *120*(6), 4719–4735. https://doi.org/10.1002/2015JA021027

Feldman, W. C., Anderson, R. C., Bame, S. J., Gary, S. P., Gosling, J. T., McComas, D. J., et al. (1983). Electron velocity distributions near the Earth's bow shock. *Journal of Geophysical Research*, *88*(A1), 96–110. https://doi.org/10.1029/JA088iA01p00096

Feldman, W. C., Barraclough, B., Fuller, K., Lawrence, D., Maurice, S., Miller, M., et al. (1999). The Lunar Prospector gamma-ray and neutron spectrometers. *Nuclear Instruments and Methods in Physics Research Section A: Accelerators, Spectrometers, Detectors and Associated Equipment*, *422*(1), 562–566. https://doi.org/10.1016/S0168-9002(98)00934-6

Futaana, Y., Barabash, S., Wieser, M., Lue, C., Wurz, P., Vorburger, A., et al. (2013). Remote energetic neutral atom imaging of electric potential over a lunar magnetic anomaly. *Geophysical Research Letters*, *40*(2), 262–266. https://doi.org/10.1002/grl.50135

Halekas, J. S., Lillis, R. J., Lin, R. P., Manga, M., Purucker, M. E., & Carley, R. A. (2010). How strong are lunar crustal magnetic fields at the surface? Considerations from a reexamination of the electron reflectometry technique. *Journal of Geophysical Research*, *115*(E3), E03006. https://doi.org/10.1029/2009JE003516

Halekas, J. S., Mitchell, D. L., Lin, R. P., Frey, S., Hood, L. L., Acuña, M. H., & Binder, A. B. (2001). Mapping of crustal magnetic anomalies on the lunar near side by the Lunar Prospector electron reflectometer. *Journal of Geophysical Research*, *106*(E11), 27841–27852. https://doi.org/10.1029/2000JE001380

Halekas, J. S., Mitchell, D. L., Lin, R. P., Hood, L. L., Acuña, M. H., & Binder, A. B. (2002). Evidence for negative charging of the lunar surface in shadow. *Geophysical Research Letters*, *29*(10), 77-1–77-4. https://doi.org/10.1029/2001GL014428

Harada, Y., Machida, S., Halekas, J. S., Poppe, A. R., & McFadden, J. P. (2013). Artemis observations of lunar dayside plasma in the terrestrial magnetotail lobe. *Journal of Geophysical Research: Space Physics*, *118*(6), 3042–3054. https://doi.org/10.1002/jgra.50296

Hemingway, D., & Garrick-Bethell, I. (2012). Magnetic field direction and lunar swirl morphology: Insights from Airy and Reiner Gamma. *Journal of Geophysical Research*, *117*(E10), E10012. https://doi.org/10.1029/2012JE004165

Jarvinen, R., Alho, M., Kallio, E., Wurz, P., Barabash, S., & Futaana, Y. (2014). On vertical electric fields at lunar magnetic anomalies. *Geophysical Research Letters*, *41*(7), 2243–2249. https://doi.org/10.1002/2014GL059788

Kaguya-project. (2017). Datasets of SELENE (KAGUYA) observations [Dataset]. *JAXA*. Retrieved from https://data.darts.isas.jaxa.jp/pub/pds3/

Kato, M., Harada, Y., Saito, Y., Yokota, S., Nishino, M. N., Takahashi, F., et al. (2024). Data for 'inhomogeneous electrostatic potentials on the dayside lunar surface in the terrestrial magnetotail lobes: The role of lunar crustal magnetic fields' [Dataset]. *Masahisa Kato*. Retrieved from http://hdl.handle.net/2433/290305

Kato, M., Harada, Y., Xu, S., Poppe, A. R., Halekas, J. S., Miyake, Y., et al. (2023). Modeling photoelectron and auger electron emission from the sunlit lunar surface: A comparison with ARTEMIS observations. *Journal of Geophysical Research: Space Physics*, *128*(10), e2023JA031707. https://doi.org/10.1029/2023JA031707

Kato, M., Sasaki, S., Takizawa, Y., & Team, K. P. (2010). The Kaguya mission overview. *Space Science Reviews*, *154*(1–4), 3–19. https://doi.org/10.1007/s11214-010-9678-3

Lin, R. P., & Gopalan, R. (1991). Mapping the composition of planetary surfaces by Auger electron spectroscopy. *Review of Scientific Instruments*, *62*(3), 660–666. https://doi.org/10.1063/1.1142064

Mitchell, D. L., Halekas, J. S., Lin, R. P., Frey, S., Hood, L. L., Acuña, M. H., & Binder, A. (2008). Global mapping of lunar crustal magnetic fields by Lunar Prospector. *Icarus*, *194*(2), 401–409. https://doi.org/10.1016/j.icarus.2007.10.027

Poppe, A. R., Halekas, J. S., Delory, G. T., & Farrell, W. M. (2012). Particle-in-cell simulations of the solar wind interaction with lunar crustal magnetic anomalies: Magnetic cusp regions. *Journal of Geophysical Research*, *117*(A9), A09105. https://doi.org/10.1029/2012JA017844

Prettyman, T., Feldman, W., Lawrence, D., McKinney, G., Binder, A., Elphic, R., et al. (2002). Library least squares analysis of Lunar Prospector gamma-ray spectra. In *Paper presented at the 33rd Lunar and Planetary Science Conference*. Retrieved from https://ui.adsabs.harvard.edu/abs/2002LPI….33.2012P

Saito, Y., Nishino, M. N., Fujimoto, M., Yamamoto, T., Yokota, S., Tsunakawa, H., et al. (2012). Simultaneous observation of the electron acceleration and ion deceleration over lunar magnetic anomalies. *Earth, Planets and Space*, *64*(2), 4–92. https://doi.org/10.5047/eps.2011.07.011

Saito, Y., Yokota, S., Asamura, K., Tanaka, T., Akiba, R., Fujimoto, M., et al. (2008). Low-energy charged particle measurement by MAP-PACE onboard SELENE. *Earth, Planets and Space*, *60*(4), 375–385. https://doi.org/10.1186/bf03352802

Speyerer, E., Robinson, M., Denevi, B., & LROC Science Team. (2011). Lunar Reconnaissance Orbiter Camera global morphological map of the Moon. In *42nd Annual Lunar and Planetary Science Conference* (p. 2387).

Usui, H., Miyake, Y., Nishino, M. N., Matsubara, T., & Wang, J. (2017). Electron dynamics in the minimagnetosphere above a lunar magnetic anomaly. *Journal of Geophysical Research: Space Physics*, *122*(2), 1555–1571. https://doi.org/10.1002/2016JA022927

Vorburger, A., Wurz, P., Barabash, S., Wieser, M., Futaana, Y., Holmström, M., et al. (2012). Energetic neutral atom observations of magnetic anomalies on the lunar surface. *Journal of Geophysical Research*, *117*(A7), A07208. https://doi.org/10.1029/2012JA017553

Whipple, E. C. (1981). Potentials of surfaces in space. *Reports on Progress in Physics*, *44*(11), 1197–1250. https://doi.org/10.1088/0034-4885/44/11/002

Xu, S., Poppe, A. R., Harada, Y., Halekas, J. S., & Chamberlin, P. C. (2021). Lunar photoemission yields inferred from ARTEMIS measurements. *Journal of Geophysical Research: Planets*, *126*(6), e2020JE006790. https://doi.org/10.1029/2020JE006790

Yeo, L. H., Han, J., Wang, X., Werner, G., Deca, J., Munsat, T., & Horányi, M. (2022). Laboratory simulation of solar wind interaction with lunar magnetic anomalies. *Journal of Geophysical Research: Space Physics*, *127*(1), e2021JA029821. https://doi.org/10.1029/2021JA029821